Journal of Colloid and Interface Science 529 (2018) 111–121

Contents lists available at ScienceDirect

Journal of Colloid and Interface Science

journal homepage: www.elsevier.com/locate/jcis

Regular Article

Solvothermal synthesis, characterization and photocatalytic property of zirconium dioxide doped titanium dioxide spinous hollow microspheres with sunflower pollen as bio-templates

Junkai Zhao [a], Shengsong Ge [a,*], Duo Pan [a], Qian Shao [a], Jing Lin [b,*], Zhikang Wang [c], Zhen Hu [d,*], Tingting Wu [e], Zhanhu Guo [f,*]

[a] College of Chemical and Environmental Engineering, Shandong University of Science and Technology, Qingdao 266590, China
[b] School of Chemistry and Chemical Engineering, Guangzhou University, Guangzhou 510006, China
[c] College of Eco-environmental Engineering, Guizhou Minzu University, Guiyang, Guizhou 550025, China
[d] School of Chemistry and Chemical Engineering, MIIT Key Laboratory of Critical Materials Technology for New Energy Conversion and Storage, Harbin Institute of Technology, Harbin 150001, China
[e] Department of Civil and Environmental Engineering, The University of Alabama, Huntsville, AL 35899, USA
[f] Integrated Composites Laboratory (ICL), Department of Chemical & Biomolecular Engineering, University of Tennessee, Knoxville, TN 37996, USA

GRAPHICAL ABSTRACT

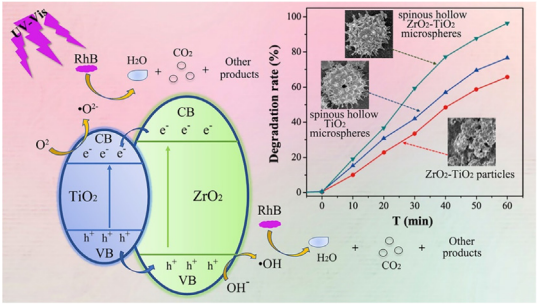

ARTICLE INFO

Article history:
Received 26 February 2018
Revised 23 May 2018
Accepted 25 May 2018
Available online 28 May 2018

Keywords:
ZrO_2 doped TiO_2 hollow microspheres
Bio-template
Solvothermal method
Photocatalytic
Mechanism analysis

ABSTRACT

Zirconium dioxide (ZrO_2) doped titanium dioxide (TiO_2) spinous hollow microspheres were successfully prepared through a facile solvothermal method using sunflower pollen as bio-templates. The products were characterized by scanning electron microscopy (SEM), X-ray diffraction (XRD), X-ray photoelectron spectroscopy (XPS), Fourier transform infrared spectroscopy (FT-IR), N_2 adsorption–desorption isotherms and UV–Vis diffuse reflectance spectroscopy. It was found that the products have spinous microsphere morphology with an approximate diameter of 12 μm. The ZrO_2 doped TiO_2 hollow microspheres exhibited a higher photocatalytic activity in the degradation of Rhodamine B (RhB) in aqueous solutions under UV-light irradiation compared with TiO_2 hollow microspheres and ZrO_2-doped TiO_2 particles. In particular, the removal of RhB followed pseudo-first-order kinetics, and 96.3% of RhB was degraded in 60 min under UV-light irradiation when ZrO_2 doped TiO_2 spinous hollow microspheres were used as the photocatalysts. Neutral and alkaline conditions were found to favor over acidic conditions for the photocatalytic degradation of RhB. Furthermore, scavenging experiments indicated that photogenerated holes (h^+) and radicals ($\cdot OH$ and $\cdot O_2^-$) were the main reactive species in the photocatalytic process using ZrO_2 doped TiO_2 hollow microspheres as the catalysts under UV light irradiation.

* Corresponding authors.
E-mail addresses: geshengsong@126.com (S. Ge), linjing@gzhu.edu.cn (J. Lin), huzhen@hit.edu.cn (Z. Hu), zguo10@utk.edu (Z. Guo).

https://doi.org/10.1016/j.jcis.2018.05.091
0021-9797/

1. Introduction

With the increasingly widespread application of organic dyes in industries, printing and dyeing wastewater containing a high content of dye pollutants poses a serious threat to the environment [1]. Many treatment methods, such as biodegradation, adsorption, ozonolysis, and photocatalysis, have been used to alleviate the environmental burden caused by dye pollutants [2–8]. In particular, the photocatalytic method has attracted much attention because it is economical, efficient, and environmental friendly [9]. Titanium dioxide (TiO_2) has been widely used as photocatalysts owing to its excellent chemical stability, non-toxicity, low-cost, and reusability [10,11]. However, both low specific surface area and easy recombination of the electron (e^-)-hole (h^+) pairs of the traditional TiO_2 photocatalyst have hindered its wide applications [12]. Therefore, the development of reliable and high efficient photocatalysts that overcome these limitations is of great importance [13].

Synthesis of photocatalysts with distinctive structures is a promising way to achieve high photocatalytic activity owing to the unique morphology and high specific surface area [14]. Many structures, including hollow microsphere, hollow cube, nanotube, and nanosheet, have been reported [15–24]. Especially, TiO_2 photocatalysts with hollow structures have received great attention in recent studies. For example, He et al. synthesized mesoporous TiO_2 hollow microspheres with an excellent photocatalytic activity by using natural rape pollen as a bio-template [10]. Zhang et al. prepared hollow TiO_2 cubes with a high specific surface area up to 132 m^2/g using a hydrothermal procedure, and the catalysts showed superior performance for dye degradation in water [25]. To address the recombination of photoinduced electron-hole pairs in the photocatalytic reactions, doping with other semiconductor materials or sensitizing with certain chemical substances are the most feasible approaches to enhance the separation of electron–hole pairs [26–29]. For example, Han et al. prepared TiO_2 nanotube arrays sensitized by 5, 10, 15, 20-tetrakis (4-chlorophenyl) porphyrin (H_2TClPP-TNTs) via a facile surface adsorption method, and the as-prepared H_2TClPP-TNTs photoelectrode exhibited excellent photoelectrochemical performance and photocatalytic properties [30]. Recent studies also indicate that TiO_2 materials doped with metal oxides such as SiO_2—TiO_2, ZrO_2—TiO_2, WO_3—TiO_2, and Al_2O_3—TiO_2 possessed enhanced photocatalytic properties than pure TiO_2 [31–34].

Zirconium dioxide (ZrO_2), as a typical *n*-type semiconductor, has a wide band gap (ca. 5.0 eV) and other unique characteristics, such as weak acidity which results in slightly acidic surface of the materials doped with ZrO_2 [13]. The acidity coming from the surface hydroxyl groups can capture light-induced holes and suppress the recombination process of electron-hole pairs thus increasing the quantum yield [35]. Furthermore, the addition of appropriate amounts of ZrO_2 can decrease the crystallite size of TiO_2 due to the dissimilar nuclei and coordination geometry [36]. Consequently, the fabrication of ZrO_2—TiO_2 composite materials with special structures has attracted extensive attention. For example, Liu et al. synthesized mesoporous ZrO_2—TiO_2 composite nanoparticles through solvothermal method and demonstrated higher photocatalytic activity compared with that of the commercial P25 [29]. Li et al. prepared macro–mesoporous ZrO_2—TiO_2 composite materials by a facile surfactant self-assembly method and the photocatalytic activities of the novel composites were remarkably higher than that of the corresponding pure TiO_2 and ZrO_2 materials in the decomposition of Rhodamine B (RhB) under UV light radiation [37].

In recent years, template methods have been increasingly used to prepare products with special morphology [38–44]. Among various templates that have been used, biological templates have many advantages, such as uniform morphology, economy, and environmental friendliness. For example, Pan et al. synthesized In_2O_3 hollow microspheres using yeasts as templates via a simple co-precipitation route and further evaluated their photoelectrocatalytic performance [45]. Yang et al. synthesized spinous ZrO_2 core–shell microspheres with good hydrogen storage properties via a hydrothermal method using pollen as a bio-template [46]. In our previous work, hollow porous ZrO_2 microspheres were prepared by microwave solvothermal method using rape pollen as a template [47]. However, the synthesis of ZrO_2 doped TiO_2 spinous hollow microspheres using sunflower pollen templates has not been reported so far.

In this paper, ZrO_2 doped TiO_2 spinous hollow microspheres were successfully synthesized by a facile solvothermal method using sunflower pollen as templates. The photocatalytic performance was examined by RhB degradation in aqueous solution under UV-light irradiation. Compared with TiO_2 spinous hollow microspheres and ZrO_2-TiO_2 particles, ZrO_2 doped TiO_2 spinous hollow microspheres exhibited a higher photocatalytic performance, indicating the essential role of ZrO_2 dopant and the unique spinous hollow structure.

2. Experimental

2.1. Materials

Sunflower pollen was purchased from Yixing Shicheng Kanghuang Bee Industry Co. Ltd. (Yixing, China). Zirconium *n*-butoxide (80 wt%) and titanium butoxide were obtained from Shanghai Alading Reagent Co. Ltd. (AR, Shanghai, China). Rhodamine B (RhB) was purchased from Tianjin Bodi Chemical Reagent Co. Ltd. (AR, Tianjin, China). Isopropyl alcohol (IPA), P-benzoquinone (BQ) and triethanolamine (TEOA) were purchased from Chengdu Kelong Co. Ltd. (AR, Chengdu, China). All the reagents were of analytical grade and used without any further purification. Distilled water and absolute alcohol were used throughout the experiments.

2.2. Fabrication of TiO_2 spinous hollow microspheres

TiO_2 spinous hollow microspheres were prepared as follows: 1.0 g sunflower pollen template was dispersed into 30 mL absolute ethanol by ultrasonication for 30 min, then titanium butoxide (0.45 mL) was added under continuous magnetic stirring. After 2-h stirring, distilled water (0.45 mL) was added and then the mixture was added into a sealed Teflon-lined autoclave and heated at100 °C for 18 h. After the Teflon-lined autoclave was cooled down to room temperature, the products were collected by centrifugation and washed with distilled water and absolute ethanol for three times, respectively. Finally, the TiO_2 spinous hollow microspheres were obtained by calcining the products at 600 °C for 2 h at a ramp rate of 1.5 °C/min. and designated as T-SH.

2.3. Fabrication of ZrO_2 doped TiO_2 spinous hollow microspheres

The method for preparing ZrO_2 doped TiO_2 spinous hollow microspheres was the same as that of TiO_2 spinous hollow microspheres, except that the mixture of titanium butoxide and zirconium *n*-butoxide was added instead of titanium butoxide. The volume of distilled water added was the same as that of the mixed ester. In addition, for comparison, ZrO_2 doped TiO_2 particles were fabricated via the same method without templates. The amount of zirconium *n*-butoxide added and the corresponding abbreviations of the samples are summarized in Table 1.

Table 1
Information of different samples.

Sunflower pollen (g)	Titanium butoxide (mL)[a]	Zirconium n-butoxide (mL)[a]	Deionized water (mL)[a]	$\frac{n_{Zr}}{n_{Zr+Ti}}$[b]	Abbreviation[c]
1	0.45	0	0.45	0%	T-SH
1	0.40	0.02	0.42	4.6%	ZT-SH-1
1	0.40	0.04	0.44	8.8%	ZT-SH-2
1	0.40	0.06	0.46	12.6%	ZT-SH-3
1	0.40	0.08	0.48	16.2%	ZT-SH-4
0	0.40	0.02	0.42	4.6%	ZT-P-1
0	0.40	0.04	0.44	8.8%	ZT-P-2
0	0.40	0.06	0.46	12.6%	ZT-P-3
0	0.40	0.08	0.48	16.2%	ZT-P-4

[a] The amount of chemical reagents needed for different samples.
[b] The molar ratio of Zirconium *n*-butoxide in mixed esters.
[c] Abbreviations for different samples.

2.4. Characterization

The morphology and structural analysis of the samples were examined by a scanning electron microscope (SEM, S-4800, Hitachi, Japan). The crystal structures of the products were tested by X-ray diffraction (XRD, ultima IV, Rigaku, Japan) with Cu Kα radiation (λ = 0.154 nm) at a scanning rate of 8°/min in 2θ range from 10° to 80°. Elemental composition information of the samples was collected by an ESCALAB 250Xi X-ray photoelecton spectrometer (XPS, Thermo Scientific, USA) with a monochromatic Al K-Alpha radiation (150 W, 15 KV, and 1486 eV). Fourier transform infrared (FT-IR) spectra were measured using KBr pellet on a Fourier transform infrared spectrometer (FT-IR, Nicolet 380, Thermo, America). The UV–Vis diffuse reflectance spectra of the samples were analyzed by UV–2550 UV–Vis spectrophotometer (UV–Vis DRS, UH4150, Hitachi, Japan). The N_2 adsorption-desorption isotherms were obtained at 77.350 K using a micromeritics surface area and pore volume analyzer (TriStar II 3020, USA). Zeta potential was tested by a microiontophoresis apparatus (Powereach, JS94H, China).

2.5. Photocatalytic activity tests

The photocatalytic activity was evaluated by degradation of RhB in aqueous solutions under UV-light irradiation. Typically, 20 mg of catalyst powder was dispersed in 50 mL aqueous solution with an RhB concentration of 20 mg/L. The pH of the solution was adjusted with HCl and NaOH as needed. The suspension was magnetically stirred in dark for 1 h to obtain the adsorption-desorption equilibrium between RhB and the catalysts. Then the mixture was transferred to the photochemical reactor and irradiated under UV-light (UV lamp, 120 W, 254 nm). 2 mL solution was sampled at regular intervals and the catalysts were separated by centrifugation at 10000 rpm for 3 min. The RhB concentration was measured using

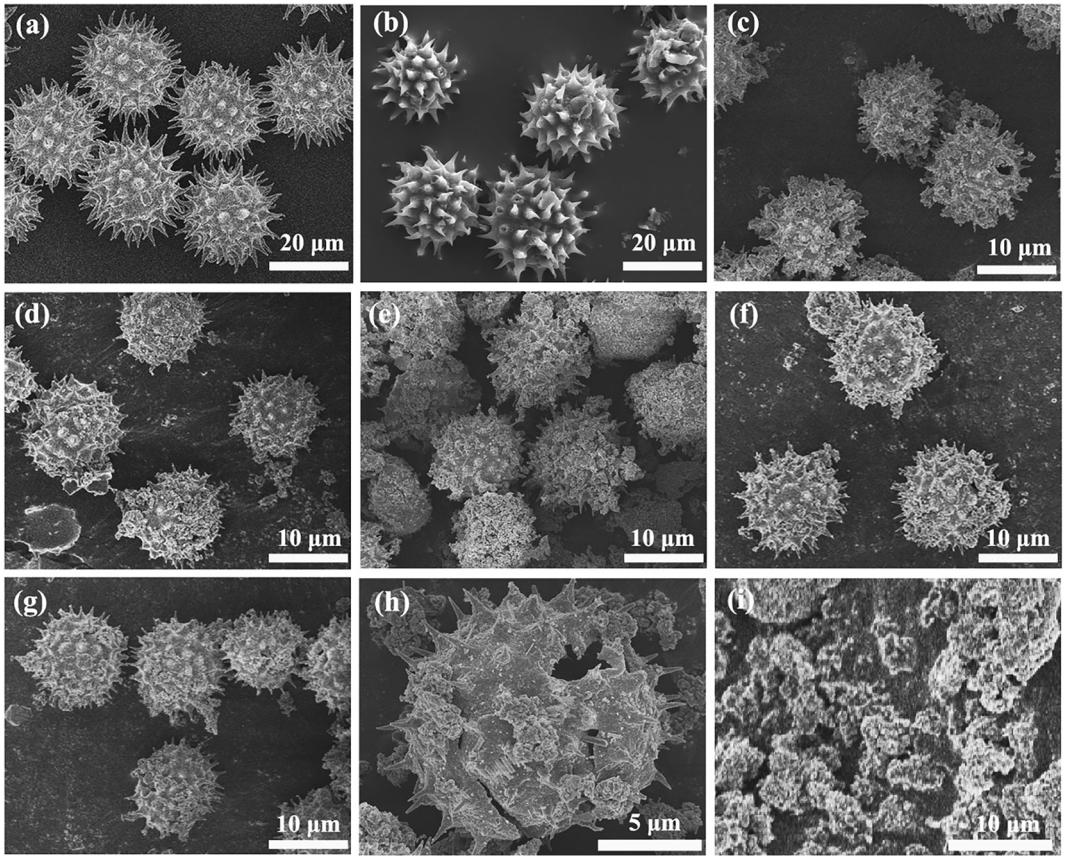

Fig. 1. SEM images of sunflower pollen (a), ZT-SH-3 before calcination (b), T-SH (c), ZT-SH-1 (d), ZT-SH-2 (e), ZT-SH-3 (f), ZT-SH-4 (g), a broken microsphere (h) and ZT-P-3 (i).

a UV–visible spectrophotometer (UH-4150) at a wavelength of 554 nm. All photocatalytic experiments were repeated three times under the same conditions.

3. Results and discussion

3.1. Characterization of the products

Fig. 1 shows the SEM images of the obtained products and sunflower pollen. The sunflower pollen is close to spherical with spines on the surface. Each pollen grain is approximately 25 μm in diameter. ZrO_2 doped TiO_2 spinous hollow microspheres before calcination have similar morphology and sizes to those of sunflower pollen (Fig. 1b). The morphologies of T-SH, ZT-SH-1, ZT-SH-2, ZT-SH-3, and ZT-SH-4 are shown in Fig. 1c, d, e and f, respectively. Although the ratio of ZrO_2 and TiO_2 varies, these samples have roughly the same morphology, and retain the spherical shape of sunflower pollen template with a spine length of 1–2 μm. Compared to the pollen, the diameter of the ZrO_2 doped TiO_2 spinous hollow microspheres is smaller (12–15 μm), which may be due to the removal of pollen template and the changes of ZrO_2 and TiO_2 crystallinity under high calcination temperatures [39,43]. Such shrinkage was also observed in other studies using pollen to prepare hollow oxides [14,28]. The hollow structure can

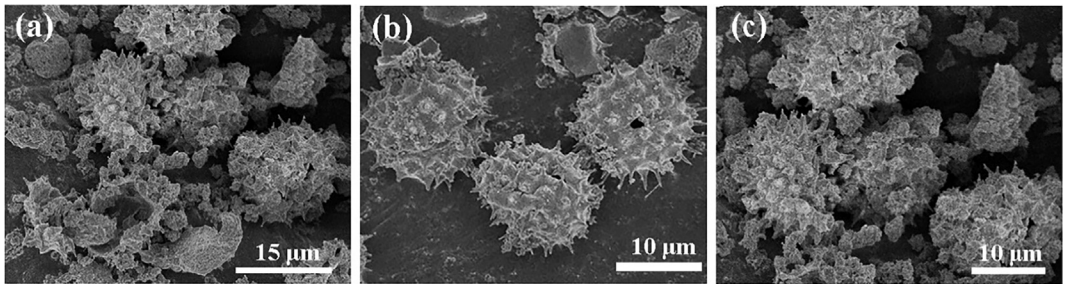

Fig. 2. SEM images of the TiO_2 spinous hollow microspheres with different amounts of Titanium butoxide: (a) 0.3 mL, (b) 0.45 mL, (c) 0.6 mL.

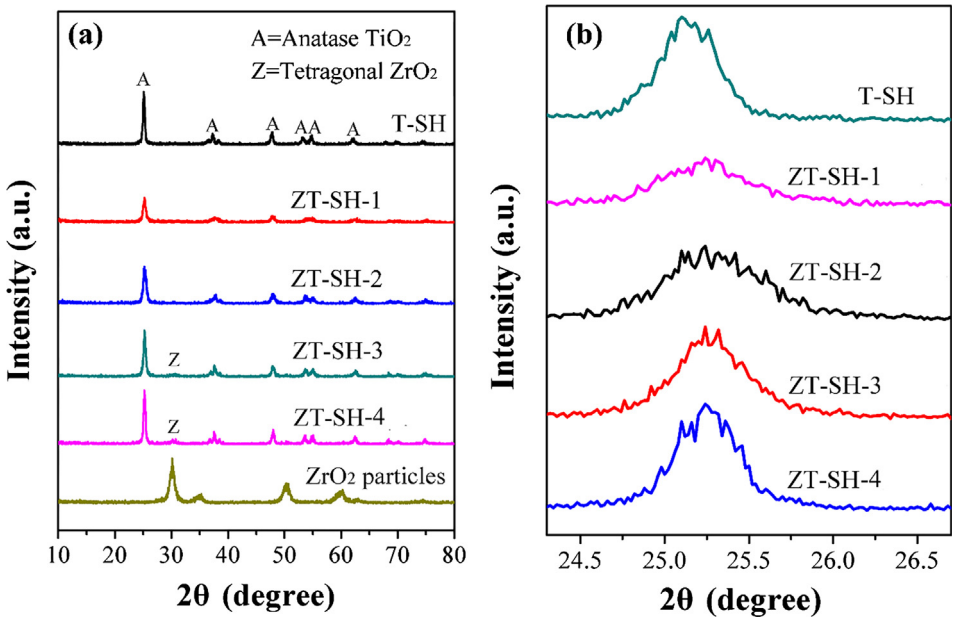

Fig. 3. (a) XRD patterns of T-SH, ZT-SH-1, ZT-SH-2, ZT-SH-3, ZT-SH-4, and ZrO_2 particles, (b) the (1 0 1) planes of T-SH, ZT-SH-1, ZT-SH-2, ZT-SH-3, and ZT-SH-4 intercepted from (a).

Table 2
Crystallite size, specific surface area, pore volume, pore diameter and band gap of samples.

Samples	D_{101} (nm)[a]	S_{BET} (m^2/g)[b]	D_{pore} (nm)[b]	V_{pore} (cm^3/g)[b]	E_g (eV)[c]
T-SH	20.4	43.41	3.7	0.20	3.28
ZT-SH-1	15.8	56.03	3.7	0.21	3.42
ZT-SH-2	17.7	56.24	3.7	0.17	3.42
ZT-SH-3	18.1	56.42	3.8	0.19	3.44
ZT-SH-4	19.7	53.22	3.8	0.16	3.44
ZT-*P*-3	/	36.21	4.1	0.18	/
ZrO_2 particles	/	/	/	/	4.96

[a] Calculated from the main peak (1 0 1) in XRD patterns shown in Fig. 3 using the Scherrer equation.
[b] Estimated by BET N_2 adsorption method (Fig. 7).
[c] Estimated by UV–vis diffuse reflectance spectra (Fig. 6).

be clearly seen from the broken microspheres (ZT-SH-3, Fig. 1h), which can be ascribed to the CO_2 release during the carbonization of organic matter in pollen [35]. As shown in Fig. 1i (ZT-P-3), the samples fabricated without templates are irregular aggregated particles. All the particle products (ZT-P-1, ZT-P-2, ZT-P-3, and ZT-P-4) share similar morphologies.

Fig. 2 shows the SEM images of TiO_2 spinous hollow microspheres prepared with different amount of titanium butoxide. As can be seen, the integrity of sunflower pollen cannot be maintained with low titanium butoxide content (0.3 mL, Fig. 2a), while severe aggregation occurred when excess titanium butoxide was added (0.6 mL, Fig. 2c). With appropriate amount of titanium butoxide, spherical, non-aggregated final products were obtained (0.45 mL, Fig. 2b). Therefore, a total volume of ~0.45 mL of zirconium *n*-butoxide and titanium butoxide (The specific amount of zirconium *n*-butoxide and titanium butoxide in Table 1) is recommended for ZrO_2 doped TiO_2 spinous hollow microspheres synthesis using the procedure reported here.

The crystallinity and crystalline phase of the as-prepared samples are shown in Fig. 3. Fig. 3a indicates that TiO_2 is present in anatase phase in all the samples, with characteristic diffraction peaks at 25.26, 36.94, 48.05, 53.89, 55.06 and 62.68° assigned to (1 0 1), (0 0 4), (2 0 0), (1 0 5), (2 1 1) and (2 0 4) crystal planes of anatase TiO_2, respectively [28,48,49]. The XRD pattern of pure ZrO_2 sample is also shown in Fig. 3a, but no characteristic diffraction peaks of ZrO_2 are observed in ZT-SH-1 and ZT-SH-2. This may be ascribed to the low amount of ZrO_2 dopant and the efficient intercalation of Zr^{4+} into the TiO_2 crystal lattice sites [35]. In contrast, a weak tetragonal crystal ZrO_2 peak at 30.32° [46] appears in ZT-SH-3 and ZT-SH-4 samples which are doped with higher amounts of ZrO_2. Fig. 3b shows the anatase (1 0 1) diffraction peaks of the ZrO_2 doped TiO_2 spinous hollow microspheres and TiO_2 spinous hollow microspheres. The crystallite size was calculated according to the Scherrer Formula: $D_{hkl} = 0.9\lambda/(\beta\cos\theta)^{-1}$ [42].

where λ is the X-ray wavelength, β is the full width at half maximum and θ is Bragg angle. The results are summarized in Table 2.

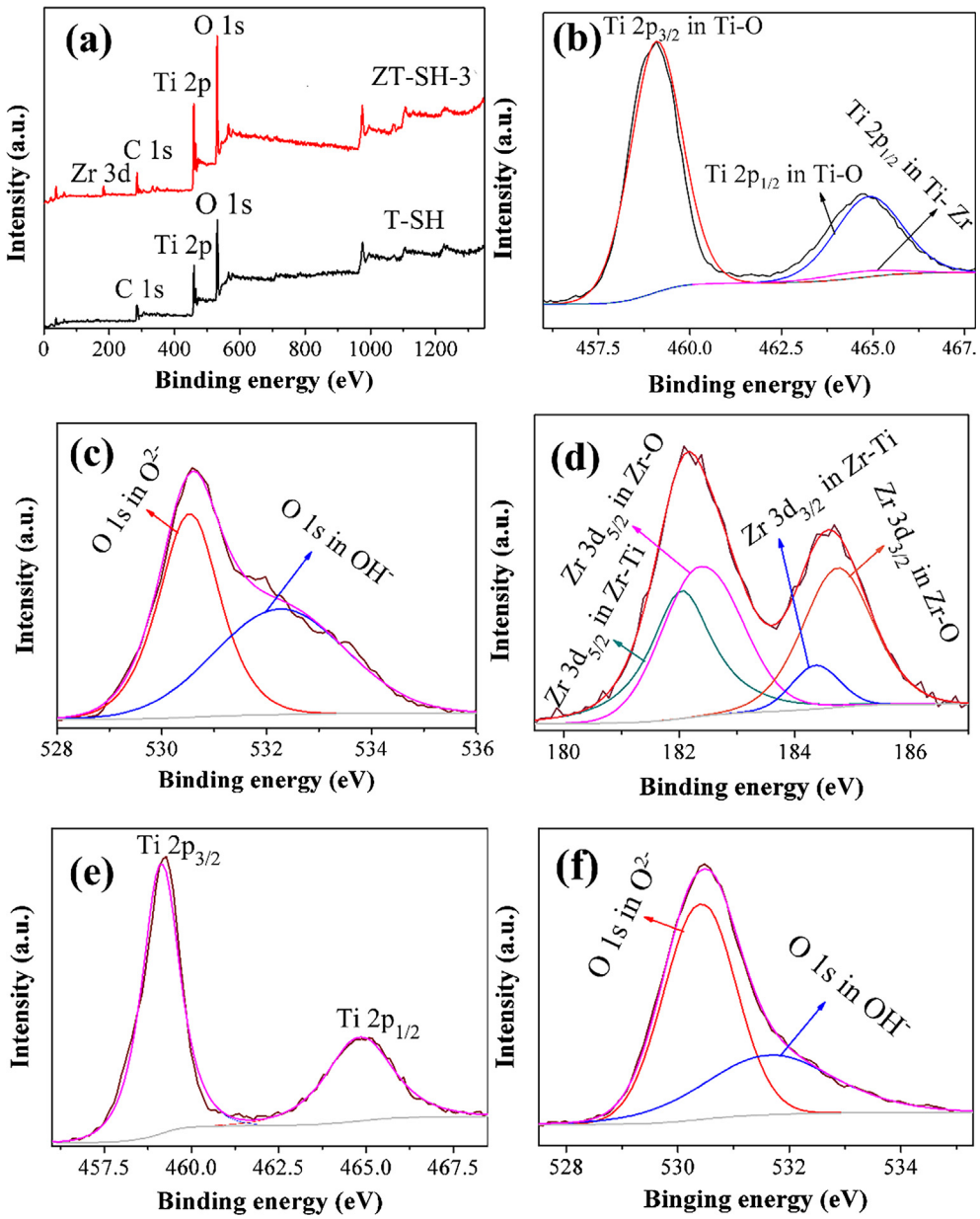

Fig. 4. XPS full survey spectra of T-SH and ZT-SH-3 (a), the XPS spectra of Ti 2p (b), O 1s (c) and Zr 3d (d) in ZT-SH-3, and Ti 2p (e) and O 1s (f) in T-SH.

Clearly, the crystal size of ZrO_2 doped TiO_2 is smaller than that of TiO_2, i.e. doping ZrO_2 in TiO_2 can decrease the crystallite size of TiO_2. This may be explained by different nuclei and coordination geometry of ZrO_2 and TiO_2 [29].

The chemical compositions of the samples are confirmed by XPS measurements, focusing on Here T-SH (control) and ZT-SH-3 (highest photocatalytic activity, Section 3.3). The XPS survey of *T*-SH and ZT-SH-3 (Fig. 4a) shows that the main elements are Ti, O, and Zr for ZT-SH-3, and Ti and O for T-SH. In addition, both samples contain carbon, which may come from the carbonization of pollen during calcination. The high-resolution Ti 2p XPS spectra of ZT-SH-3 (Fig. 4b) and T-SH (Fig. 4e) can be deconvoluted into two peaks with binding energies at 464.6 and 459.0 eV assigned to Ti^{4+} [35]. In addition, there is an inconspicuous peak at 465.2 eV, which can be attributed to the Zr—Ti chemical bonds [50]. The O 1 s peaks localized at 532.4 eV and 530.5 eV in the spectra of ZT-SH-3 (Fig. 4c) and T-SH (Fig. 4f) can be ascribed to —OH and O^{2-}, respectively [37]. The XPS spectrum of Zr 3d of ZT-SH-3 is shown in Fig. 4d, where the peaks with binding energies at 184.9 (Zr $3d_{3/2}$) and 182.8 eV (Zr $3d_{5/2}$) confirm the presence of Zr—O. [28]. The peaks at 184.5 (Zr $3d_{3/2}$) and 182.1 eV (Zr $3d_{5/2}$) can be attributed to the ≡Zr—O—Ti≡ chemical bonds [37]. The existence of ≡Zr—O—Ti≡ and Zr—Ti chemical bonds results from the phase contact between ZrO_2 and TiO_2, which indicates that ZrO_2 and TiO_2 form a homogeneous composite material [35]. The mole fraction of ZrO_2 in ZT-SH-3 is estimated to be 11.9% based on the peak area of XPS spectra (Fig. 4b and d), which is close to the theoretical value (12.6%).

The FT-IR spectra of ZT-SH-1, ZT-SH-2, ZT-SH-3 and ZT-SH-4 (Fig. 5) show a peak at 1300 cm^{-1} corresponding to the C—O stretching vibration. This may come from the carbide formed during pollen calcination [35]. The peaks at 3400 cm^{-1} (ZT-SH-1, ZT-SH-2, ZT-SH-3) and 3590 cm^{-1} (ZT-SH-4) correspond to the vibration of —OH symmetry and asymmetry stretching. The intense peak around 1630 cm^{-1} is attributed to the bending vibration of the Ti—OH bond [30]. Two distinct characteristic peaks can be seen from the infrared spectrum of the T-SH. The peak around 3290 cm^{-1} corresponds to the stretching vibration of hydroxyl and the peak at 1620 cm^{-1} indicates the existence of Ti—OH bond [35,51]. Obviously, the intensities of these peaks in ZT-SH-1, ZT-SH-2, ZT-SH-3 and ZT-SH-4 are much higher than those of T-SH, indicating that ZrO_2 doping increased the surface hydroxyl groups or water molecules. This feature can promote the e^--h^+ pair separation under UV-light irradiation by trapping the electrons produced in the conduction band, which eventually leads to the formation of surface free hydroxyl radicals (—OH), thus improving the photocatalytic capacity [35].

The UV–Vis absorption spectra of the samples are shown in Fig. 6a. Apparently, the spectra of ZT-SH-1, ZT-SH-2, ZT-SH-3, and ZT-SH-4 are quite different from those of ZrO_2 and T-SH. The band gap energy of the prepared samples was calculated by Eq. (1) [42]:

$$(Ahv)^2 = K(hv - E_g) \quad (1)$$

where E_g is the band gap energy, hv stands for photon energy. K and A represent proportionality constant and absorption coefficient, respectively. The normalized graphs of $(Ahv)^2$ for the photon energy of the samples are shown in Fig. 6b and the band gap energy of all samples is shown in Table 2. The band gap energy of ZrO_2 particles and T-SH is 4.96 and 3.28 eV, respectively. Compared with T-SH, the addition of ZrO_2 into TiO_2 can lead to a slightly higher band gap, resulting in the band gap energy of 3.42–3.45 eV for ZT-SH-1, ZT-SH-2, ZT-SH-3, and ZT-SH-4. Compared with TiO_2 spinous hollow microspheres, the slight blue shift of band gap energy in the ZrO_2 doped TiO_2 spinous hollow microspheres can be attributed to the larger band gap of ZrO_2 [48]. ZrO_2 can introduce new energy levels into the band gap of TiO_2, which provide electron capture centers and contribute to the separation of electron-hole pairs in the process of photocatalysis [13,52,53].

The specific surface area and pore size of the as-synthesized T-SH, ZT-SH-1, ZT-SH-2, ZT-SH-3, ZT-SH-4, and ZT-P-3 were determined by the nitrogen adsorption–desorption isotherm (Fig. 7).

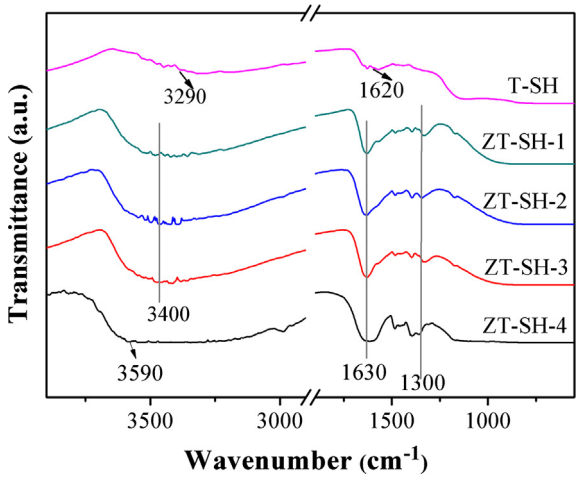

Fig. 5. FT-IR spectra of T-SH, ZT-SH-1, ZT-SH-2, ZT-SH-3, and ZT-SH-4.

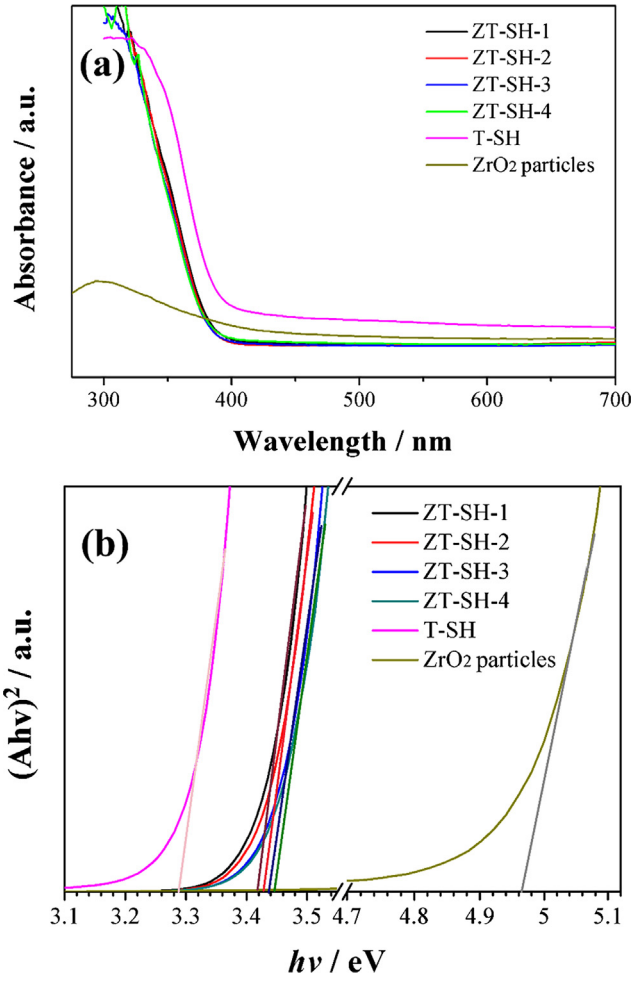

Fig. 6. UV–vis absorption spectra (a) of ZT-SH-1, ZT-SH-2, ZT-SH-3, ZT-SH-4, T-SH, and ZrO_2 particles (a), and the plot of $(Ahv)^2$ vs. hν based on the direct transition (b).

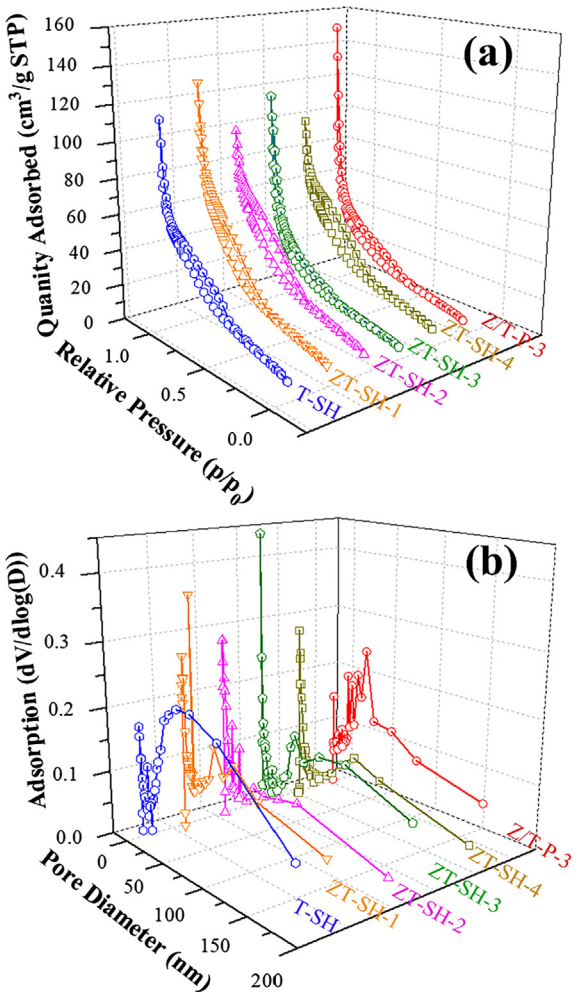

Fig. 7. Nitrogen adsorption-desorption isotherms of T-SH, ZT-SH-1, ZT-SH-2, ZT-SH-3, ZT-SH-4, and ZT-P-3 (a) and the pore size distributions of T-SH, ZT-SH-1, ZT-SH-2, ZT-SH-3, ZT-SH-4, and ZT-P-3 (b).

Fig. 7a shows that the isotherms of T-SH, ZT-SH-1, ZT-SH-2, ZT-SH-3, ZT-SH-4, and ZT-P-3 all belong to type III with a type H1 hysteresis loop [35,54]. The BET specific surface area, pore diameter, and pore volume of all samples are summarized in Table 2. Compared with ZT-P-3, the hollow samples have a larger specific surface area which can be ascribed to the hollow structure of the samples. Pore volume and pore diameter are calculated using the Barrett-Joyner-Halenda (BJH) formula. As shown in Table 2, the diameters of T-SH, ZT-SH-1, ZT-SH-2, ZT-SH-3, ZT-SH-4 and ZT-P-3 all fall in the range of 3.7–4.1 nm. Meanwhile, their pore volumes are all within the range of 0.18–0.20 cm^3/g.

3.2. Formation mechanism

From the observed SEM, FT-IR (Fig. S1) and XRD (Fig. S2) results, the formation mechanism of ZrO_2 doped TiO_2 spinous hollow microspheres is proposed in Fig. 8. Sunflower pollen with many active surface functional groups [55] can adsorb zirconium *n*-butoxide and titanium butoxide molecules through electrostatic attractions. With the addition of deionized water, Zr (IV) and Ti (IV) are transformed into ZrO_2 and TiO_2 on the pollen wall respectively under hydrothermal conditions. Finally, the ZrO_2 doped TiO_2 spinous hollow microspheres are formed after the removal of sunflower pollen through calcination at 600 °C for 2 h.

3.3. Photocatalytic activity

The photocatalytic activities of the products were evaluated by RhB degradation (pH ≈ 7) under UV light and the results are shown in Fig. 9a. First, the adsorption-desorption equilibrium between the photocatalysts and RhB can be reached in 1 h in dark. After 60 min of UV-light illumination, the RhB degradation efficiency of all the catalysts follows the order: ZT-SH-3 (96.3%) > ZT-SH-2 (90.9%) > ZT-SH-4 (88.8%) > ZT-SH-1 (80.9%) > ZT-*P*-3 (76.6%) > T-SH (65.7%) > ZrO_2 particles (14.6%). All the ZrO_2 doped TiO_2 spinous hollow microsphere samples outperformed spinous hollow TiO_2 microspheres as well as the pure ZrO_2. ZT-SH-3 exhibited the highest activity. Therefore, the addition of ZrO_2 into TiO_2 significantly improved the photocatalytic performance. The reasons for such improvement include the inhibition of the recombination of e^--h^+ pairs [52,53] and the formation of free radicals due to the surface hydroxyl groups or water molecules on zirconium doped samples [35]. Furthermore, the photocatalytic activity of hollow products (ZT-SH-3) is about 20% higher than that of the particle products (ZT-P-3) prepared with the same amount of ZrO_2 and TiO_2, due to the larger specific surface area of the former. A larger specific surface area can result in more photocatalytic active sites and accelerate the adsorption and degradation of dye molecules. [42] The time-dependent UV–Vis absorption spectra of RhB with ZT-SH-3 as the photocatalyst is shown in Fig. 9b. The digital photo (Fig. 9b, inset) shows that the RhB aqueous solution was entirely decolorized after 60 min irradiation, indicating the efficient degradation of RhB.

In order to obtain quantitative information of the photocatalytic activity of the as-prepared products, the kinetics of photocatalytic degradation of RhB was also investigated. The degradation of RhB can be described using the pseudo-first-order kinetic model as shown below [25,42]:

$$ln(C_0 - C_t) = kt \quad (2)$$

where k is the first-order apparent rate constant and t is the light irradiation time. C_0 and C_t represent the concentrations of RhB at beginning and time t, respectively. The value of the apparent rate constant k and the correlation coefficient R^2 are shown in Fig. 9c. The highest rate constant of ZT-SH-3 (0.0454 min^{-1}) is consistent with the results shown in Fig. 9a.

The effect of solution pH on the photocatalytic degradation of RhB using ZT-SH-3 is illustrated in Fig. 9d. More than 95% of RhB was degraded when pH was higher than 7. In contrast, 83% and 73% were degraded at pH 5 and 3, respectively. The solution pH can affect the electrical properties of the catalyst particles (Fig. S3), and further affect the adsorption of dye molecules and

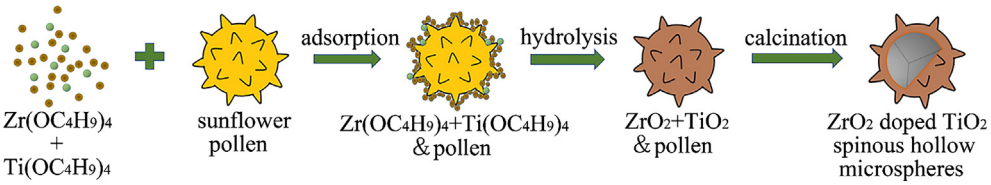

Fig. 8. Schematic illustration of the formation of ZrO_2 doped TiO_2 spinous hollow microspheres.

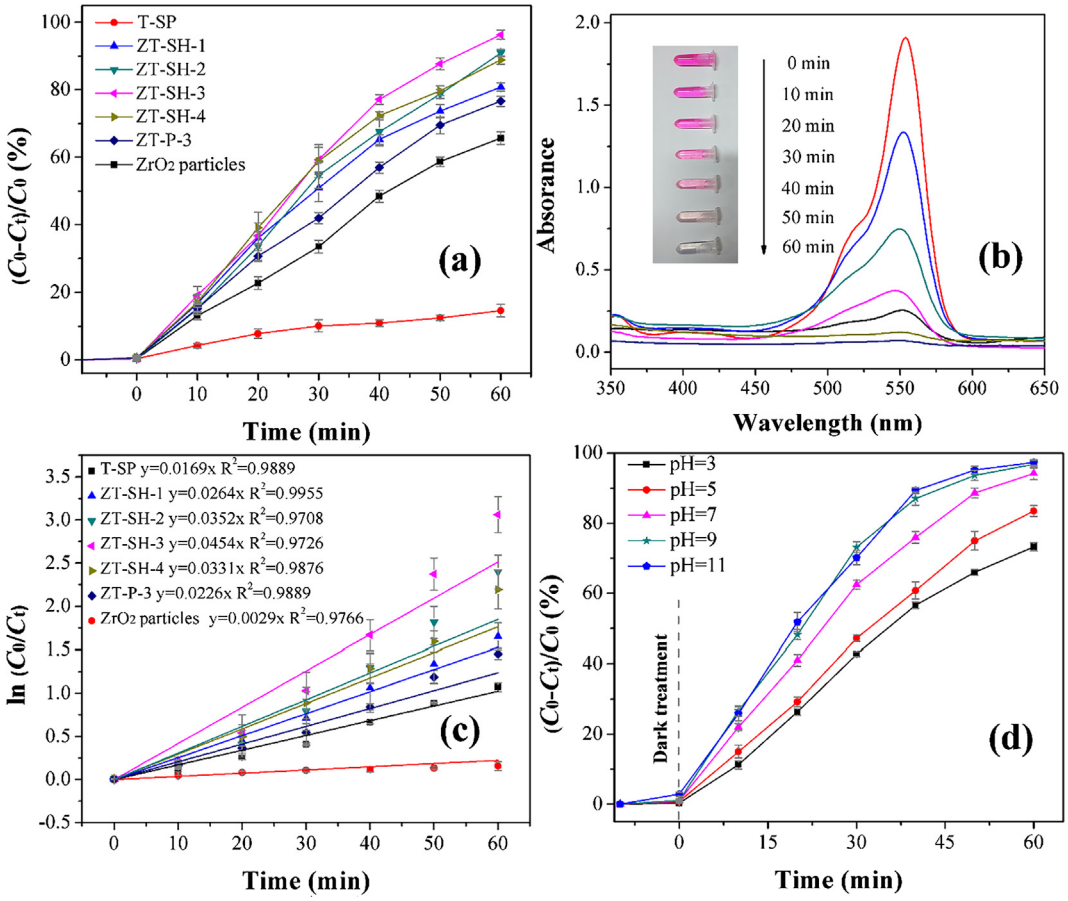

Fig. 9. Photocatalytic degradation of RhB using ZrO_2 doped TiO_2 spinous hollow microspheres under UV-light irradiation (a), the time-dependent UV–vis absorption spectra of RhB with ZT-SH-3 as photocatalyst (b), the photodegradation kinetic curves of samples (c) and the effect of pH on the photocatalytic degradation of RhB with ZT-SH-3 as photocatalyst (d).

consequently the degradation efficiency [35,36,56]. Although the photocatalytic activity of ZrO_2 doped TiO_2 spinous hollow microspheres under acidic conditions is weaker than that under neutral and alkaline conditions, more than 70% removal achieved under all conditions indicates that the ZrO_2 doped TiO_2 spinous hollow microspheres can effectively degrade the dye pollutants within a wide pH range.

The reusability of ZT-SH-3 was tested in the recycling experiments. As shown in Fig. 10, ZT-SH-3 maintained high photocatalytic activities even after 6 cycles. Moreover, ZT-SH-3 can still maintain its initial morphology after multiple cycles (Fig. 10b and c). These results indicate the high physical stability and reusability of ZT-SH-3.

To elucidate the photocatalytic mechanism of ZT-SH-3 and probe the active species in the photocatalytic process, h^+, $\cdot O_2^-$, and ·OH scavengers were added in the trapping experiments, where isopropyl alcohol (IPA; 1 mM), p-benzoquinone (BQ; 1 mM), and triethanolamine (TEOA; 1 mM) were used as the hydroxyl radical, superoxide radical, and hole quenchers, respectively [50]. As can be seen in Fig. 11, the addition of TEOA, BQ, and IPA significantly inhibited the RhB degradation, resulting in less than 50% removal, indicating that h^+, ·OH, and $\cdot O_2^-$ radicals all contributed to the photocatalytic degradation of dyes [37]. The e^- and h^+ transfer behaviors during the photocatalytic process were illustrated in Scheme 1. The reaction process can be represented in Eqs. (3)–(11) [13,30].

$$TiO_2 \xrightarrow{UV-Vis} TiO_2(e^- + h^+) \quad (3)$$

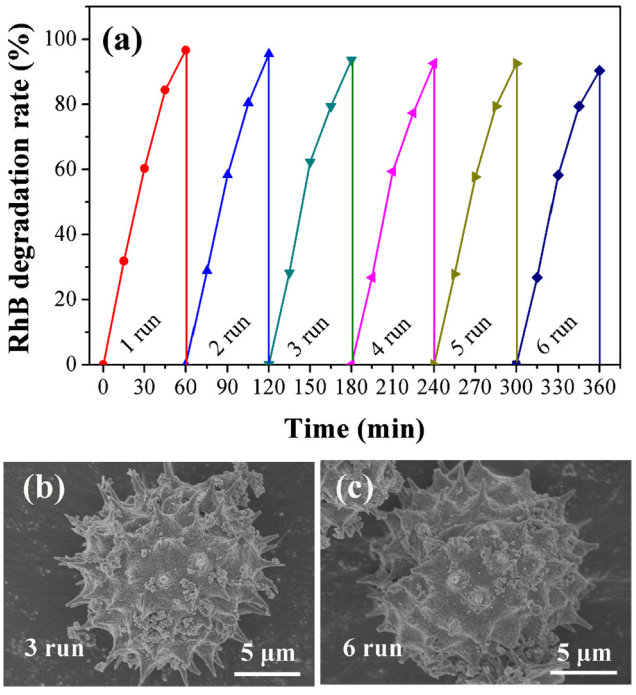

Fig. 10. Cycling runs for the photodegradation of RhB over ZT-SH-3 (a), SEM image of ZT-SH-3 after 3 cycles (b) and 6 cycles (c).

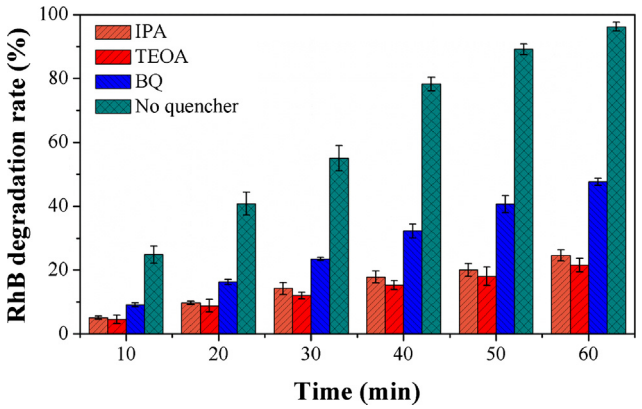

Fig. 11. Photocatalytic degradation of RhB over ZT-SH-3 with the addition of quenchers.

$$ZrO_2 \xrightarrow{UV-Vis} ZrO_2(e^- + h^+) \quad (4)$$

$$TiO_2(e^-)+O_2 \rightarrow TiO_2+\cdot O^-_2 \quad (5)$$

$$ZrO_2(e^-)+O_2 \rightarrow ZrO_2+\cdot O^-_2 \quad (6)$$

$$TiO_2(h^+)+H_2O \rightarrow TiO_2+\cdot OH+H^+ \quad (7)$$

$$TiO_2(h^+)+OH^- TiO_2+\cdot OH \quad (8)$$

$$ZrO_2(h^+)+H_2O \rightarrow ZrO_2+\cdot OH+H^+ \quad (9)$$

$$ZrO_2(h^+)+OH^- \rightarrow ZrO_2+\cdot OH \quad (10)$$

$$\begin{pmatrix} \cdot O^-_2 \\ \cdot OH \\ h^+ \end{pmatrix} + \text{Rhb} \rightarrow CO_2 + H_2O + \text{other Products} \quad (11)$$

Under UV-light irradiation, the photogenerated holes (h^+) and electrons (e^-) are in their valence band (VB) and conduction band (CB), respectively (Eqs. (3) and (4)) [57,58]. e^- and h^+ can convert O_2 and —OH in water into $\cdot O^-_2$ and ·OH respectively (Eqs.(5)–(10)). These active species ($\cdot O^-_2$, ·OH, and h^+) with strong oxidizing properties can oxidize RhB to CO_2, H_2O and other transformation products (Eqs. (11)). However, as both charge separation and charge recombination can occur simultaneously, the efficiency of photocatalysis is determined by the competition between these two process. For ZrO_2 doped TiO_2 spinous hollow microspheres, a small number of electrons can be excited to CB of ZrO_2 and be drifted to CB of TiO_2. At the same time, the positive hole centers (h^+) from TiO_2 are trapped in the VB of ZrO_2, therefore, the electron-hole pair recombination may be inhibited [35].

4. Conclusions

ZrO_2 doped TiO_2 spinous hollow microspheres with excellent photocatalytic properties were prepared through solvothermal process. The preparation method was facile with low cost and the morphology of the final product was controllable. The as-prepared ZrO_2 doped TiO_2 spinous hollow microspheres with a uniform diameter of 12–15 μm exhibited higher photocatalytic activities than that of TiO_2 spinous hollow microspheres and ZrO_2 doped TiO_2 nanoparticles. 96.3% of RhB was degraded after 60 min UV light irradiation using ZrO_2 doped TiO_2 spinous hollow microsphere as the photocatalyst. The dye degradation followed a pseudo-first-order kinetics and h^+, ·OH, and $\cdot O^-_2$ were found to be

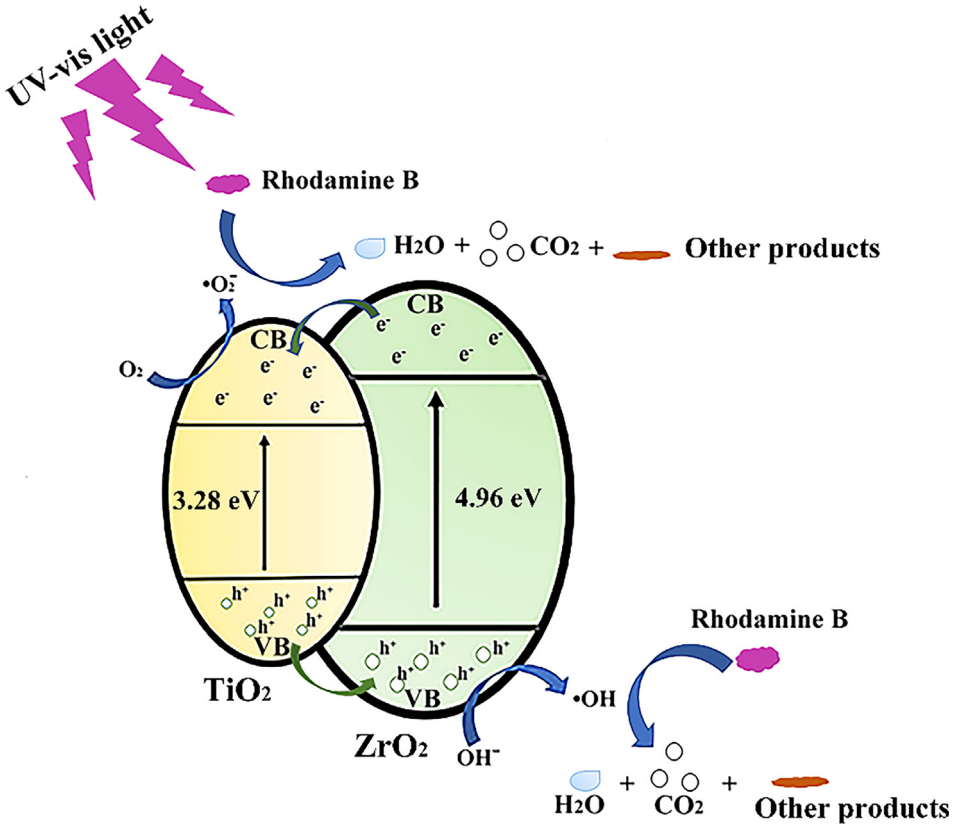

Scheme 1. Schematic illustration of the mechanism of photocatalytic RhB degradation with ZrO_2 doped TiO_2 spinous hollow microspheres as the catalysts.

the main active species. Furthermore, ZrO_2 doped TiO_2 spinous hollow microspheres exhibited satisfactory performance under both acid and alkaline conditions and good reusability. This biotemplate strategy may be further extended to the preparation of other hollow structure composites such as carbon and ceramic oxide based composites for other potential applications including electromagnetic interference (EMI) shielding [21,59–61], sensing and functional structural materials; and energy storage [62–71].

Appendix A. Supplementary material

Supplementary data associated with this article can be found, in the online version, at https://doi.org/10.1016/j.jcis.2018.05.091.

References

[1] L. Niu, Q. Zhang, J. Liu, J. Qian, X. Zhou, TiO_2 nanoparticles embedded in hollow cube with highly exposed 001 facets: facile synthesis and photovoltaic applications, J. Alloy. Compd. 656 (2016) 863–870.

[2] S. Ledakowicz, M. Solecka, R. Zylla, Biodegradation, decolourisation and detoxification of textile wastewater enhanced by advanced oxidation processes, J. Biotechnol. 89 (2001) 175–184.

[3] A. Geethakarthi, B.R. Phanikumar, Adsorption of reactive dyes from aqueous solutions by tannery sludge developed activated carbon: kinetic and equilibrium studies, Int. J. Environ. Sci. Te 8 (2011) 561–570.

[4] J. Ahmad, K. Majid, In-situ synthesis of visible-light responsive Ag_2O/graphene oxide nanocomposites and effect of graphene oxide content on its photocatalytic activity, Adv. Compos. Hybrid Mater. (2018), https://doi.org/10.1007/s42114-018-0025-6. in press.

[5] S.D. Perera, R.G. Mariano, K. Vu, N. Nour, O. Seitz, Y. Chabal, K. Balkus, Hydrothermal synthesis of graphene-TiO_2 nanotube composites with enhanced photocatalytic activity, ACS Catal. 2 (2012) 949–956.

[6] L. Zhang, M. Qin, W. Yu, Q. Zhang, H. Xie, Z. Sun, Q. Shao, X. Guo, L. Hao, Y. Zheng, Z. Guo, Heterostructured TiO_2/WO_3 nanocomposites for photocatalytic degradation of toluene under visible light, J. Electrochem. Soc. 164 (2018) H1086–H1090.

[7] Z. Sun, L. Zhang, F. Dang, Y. Liu, Z. Fei, Q. Shao, H. Lin, J. Guo, L. Xiang, N. Yerra, Z. Guo, Experimental and simulation understanding of morphology controlled barium titanate nanoparticles under co-adsorption of surfactants, CrystEngComm 19 (2017) 3288–3298.

[8] B. Song, H. Sun, Q. Shao, J. Zhao, K. Song, L. Hao, L. Wang, Z. Guo, Two-step hydrothermally synthesized carbon nanodots/WO_3 photocatalysts with enhanced photocatalytic performance, Dalton Trans. 46 (2017) 15769–15777.

[9] L. Zhang, Q. Zhang, H. Xie, J. Guo, H. Lyu, Y. Li, Z. Sun, H. Wang, Z. Guo, Electrospun titania nanofibers segregated by graphene oxide for improved visible light photocatalysis, Appl. Catal. B-Environ. 201 (2017) 470–478.

[10] H. Zhao, W. Deng, Y. Li, Atomic layer deposited TiO_2 ultrathin layer on Ag_ZnO nanorods for stable and efficient photocatalytic degradation of RhB, Adv. Compos. Hybrid Mater. (2018), https://doi.org/10.1007/s42114-017-0015-0. in press.

[11] H. Kang, Z. Cheng, H. Lai, H. Ma, Y. Liu, X. Mai, Y. Wang, Q. Shao, L. Xiang, X. Guo, Z. Guo, Superlyophobic anti-corrosive and self-cleaning titania robust mesh membrane with enhanced oil/water separation, Separat. Purificat. Technol. 201 (2018) 193–204.

[12] M.V. Dozzi, S. Marzorati, M. Longhi, M. Coduri, L. Artiglia, E. Selli, Photocatalytic activity of TiO_2-WO_3, mixed oxides in relation to electron transfer efficiency, Appl. Catal. B-Environ. 186 (2016) 157–165.

[13] B.M. Pirzada, N.A. Mir, N. Qutub, O. Mehraj, S. Sabir, Synthesis, characterization and optimization of photocatalytic activity of TiO_2/ZrO_2 nanocomposite heterostructures, Mat. Sci. Eng. B-Adv. 193 (2015) 137–145.

[14] X. Yang, B. Xu, X. Zhang, X. Song, R. Chen, Preparation of micro/nanostructure TiO_2 spheres by controlling pollen as hard template and soft template, J. Nanosci. Nanotechnol 14 (2014) 7228–7233.

[15] M. Ye, Z. Chen, W. Wang, J. Shen, J. Ma, Hydrothermal synthesis of TiO_2 hollow microspheres for the photocatalytic degradation of 4-chloronitrobenzene, J. Hazard. Mater. 184 (2010) 612–619.

[16] S. Yu, B. Liu, W. Qin, Y. Gao, S. Ying, F. Xue, X. An, L. Liu, J. Zhang, Ionic liquid assisted chemical strategy to TiO_2 hollow nanocube assemblies with surface-fluorination and nitridation and high energy crystal facet exposure for enhanced photocatalysis, ACS Appl. Mater. Interf. 6 (2014) 10283–10295.

[17] X. Cui, G. Zhu, Y. Pan, Q. Shao, C. Zhao, M. Dong, Y. Zhang, Z. Guo, Polydimethylsiloxane-titania nanocomposite coating: fabrication and corrosion resistance, Polymer 138 (2018) 203–210.

[18] S. Ding, J.S. Chen, D. Luan, F.Y. Boey, S. Madhavi, X. Lou, Graphene-supported anatase TiO_2 nanosheets for fast lithium storage, Chem. Commun. 47 (2011) 5780–5782.

[19] K. Sun, P. Xie, Z. Wang, T. Su, Q. Shao, J.E. Ryu, X. Zhang, J. Guo, A. Shankar, J. Li, R. Fan, D. Cao, Z. Guo, Flexible polydimethylsiloxane/multi-walled carbon nanotubes membranous metacomposites with negative permittivity, Polymer 125 (2017) 50–57.

[20] Y. He, S. Yang, H. Liu, Q. Shao, Q. Chen, C. Lu, Y. Jiang, C. Liu, Z. Guo, Reinforced carbon fiber laminates with oriented carbon nanotube epoxy nanocomposites: magnetic field assisted alignment and cryogenic temperature mechanical properties, J. Colloid Interf. Sci. 517 (2018) 40–51.

[21] K. Zhang, G. Li, L. Feng, N. Wang, J. Guo, K. Sun, K. Yu, J. Zeng, T. Ling, Z. Guo, M. Wang, Ultralow percolation threshold and enhanced electromagnetic interference shielding in poly(L-lactide)/multi-walled carbon nanotubes nanocomposites with electrically conductive segregated networks, J. Mater. Chem. C 5 (2017) 9359–9369.

[22] M. Zhao, L. Meng, L. Ma, et al., Layer-by-layer grafting CNTs onto carbon fibers surface for enhancing the interfacial properties of epoxy resin composites, Compos. Sci. Technol. 154 (2018) 28–36.

[23] C. Hu, Z. Li, Y. Wang, J. Gao, K. Dai, G. Zheng, C. Liu, C. Shen, H. Song, Z. Guo, Comparative assessment of the strain-sensing behaviors of polylactic acid nanocomposites: reduced graphene oxide or carbon nanotubes, J. Mater. Chem. C 5 (2017) 2318–2328.

[24] C. Lin, C. Cheng, K. Sun, X. Guo, Q. Shao, J. Li, N. Wang, Z. Guo, Nano-$TiNb_2O_7$/carbon nanotubes composite anode for enhanced lithium-ion storage, Electrochim. Acta 260 (2018) 65–72.

[25] Y. Zhang, Z.A. Qiao, J. Liu, X. Wang, S. Yao, T. Wang, B. Liu, Y. Ma, Y. Liu, Q. Huo, Ti(IV) oxalate complex-derived hierarchical hollow TiO_2 materials with dye degradation properties in water, Dalton Trans. 45 (2016) 265–270.

[26] L. Yan, H. Wang, D. Huang, H. Luo, Electrodes with high conductivities for high performance lithium/sodium ion batteries, Eng. Sci. 1 (2018) 4–20.

[27] J. Joo, S.G. Kwon, T. Yu, M. Cho, J. Lee, J. Yoon, T. Hyeon, Large-scale synthesis of TiO_2 nanorods via nonhydrolytic sol-gel ester elimination reaction and their application to photocatalytic inactivation of e. coli, J. Phys. Chem. B 109 (2005) 15297–15302.

[28] D. Bu, H. Zhuang, Synthesis, characterization, and photocatalytic studies of copper-doped TiO_2 hollow spheres using rape pollen as a novel biotemplate, Catal. Commun. 29 (2012) 24–28.

[29] H.L. Shindume, Z. Zhao, N. Wang, H. Liu, A. Umar, J. Zhang, T. Wu, Z. Guo, Enhanced photocatalytic activity of B, N-codoped TiO_2 by a new molten nitrate process, J. Nanosci. Nanotechnol. (2018), https://doi.org/10.1166/jnn.2018.15745. in press.

[30] C. Han, Q. Shao, M. Liu, S. Ge, Q. Liu, J. Lei, 5,10,15,20-tetrakis (4-chlorophenyl) porphyrin decorated TiO_2 nanotube arrays: composite photoelectrodes for visible photocurrent generation and simultaneous degradation of organic pollutant, Mat. Sci. Semicon. Proc. 56 (2016) 166–173.

[31] X. Chen, X. Wang, X. Fu, Hierarchical macro/mesoporous TiO_2/SiO_2 and TiO_2/ZrO_2 nanocomposites for environmental photocatalysis, Energy Environ. Sci 2 (2009) 872–877.

[32] K.R. Gota, S. Suresh, Preparation and its application of TiO_2/ZrO_2 and TiO_2/Fe photocatalysts: a perspective study, Asian J. Chem 26 (2014) 7081–7101.

[33] L. Zhang, M. Qin, W. Yu, Q. Zhang, H. Xie, Z. Sun, Q. Shao, X. Guo, L. Hao, Y. Zheng, Z. Guo, Heterostructured TiO_2/WO_3 nanocomposites for photocatalytic degradation of toluene under visible light, J. Electrochem. Soc. 164 (2017) 1086–1090.

[34] M. Polat, A.M. Soylu, D.A. Erdogan, H. Erguven, E.I. Vovk, E. Ozensoy, Influence of the sol–gel preparation method on the photocatalytic NO oxidation performance of TiO_2/Al_2O_3 binary oxides, Catal. Today 241 (2015) 25–32.

[35] T.V.L. Thejaswini, D. Prabhakaran, M.A. Maheswari, Synthesis of mesoporous worm-like ZrO_2–TiO_2 monoliths and their photocatalytic applications towards organic dye degradation, J. Photoch. Photobio. A 344 (2017) 212–222.

[36] A. Kambur, G.S. Pozan, I. Boz, Preparation, characterization and photocatalytic activity of TiO_2–ZrO_2 binary oxide nanoparticles, Appl. Catal. B-Environ. 115 (2012) 149–158.

[37] M. Li, X. Li, G. Jiang, G. He, Hierarchically macro–mesoporous ZrO_2–TiO_2 composites with enhanced photocatalytic activity, Ceram. Int. 41 (2015) 5749–5757.

[38] J. Huang, X. Wang, Z.L. Wang, Controlled replication of butterfly wings for achieving tunable photonic properties, Nano Lett. 6 (2006) 2325–2331.

[39] W. Zhu, S. Ge, Q. Shao, Adsorption properties of ZrO_2 hollow microboxes prepared using $CaCO_3$ cubes as templates, RSC Adv. 6 (2016) 81736–81743.

[40] S. Ge, L. Bao, Q. Shao, Q. Zhang, Q. Liu, Synthesis and visible-light photocatalytic activity of CeO_2 nanoboxes based on Pearson's principle, J. Nanosci. Nanotechnol. 17 (2017) 833–836.

[41] T. Wu, Q. Shao, S. Ge, Q. Liu, Influence of molecular weight of chitosan on the microstructures and photocatalytic property of ZrO_2 prepared by chitosan templates method, Mater. Res. Bull. 83 (2016) 657–663.

[42] B. Zhao, Q. Shao, L. Hao, L. Zhen, B. Zhang, S. Ge, L. Zhang, Yeast-template synthesized Fe-doped cerium oxide hollow microspheres for visible photodegradation of acid orange 7, J. Colloid Interf. Sci. 511 (2017) 39–47.

[43] J. Tian, Q. Shao, X. Dong, J. Zheng, D. Pan, X. Zhang, H. Cao, L. Hao, J. Liu, X. Mai, Z. Guo, Bio-template synthesized NiO/C hollow microspheres with enhanced Li-ion battery electrochemical performance, Electrochim. Acta 261 (2018) 236–245.

[44] T. Su, Q. Shao, Z. Qin, Z. Guo, Z. Wu, Role of interfaces in two-dimensional photocatalyst for water splitting, ACS Catal. 8 (2018) 2253–2276.

[45] D. Pan, S. Ge, X. Zhang, X. Mai, S. Li, Z. Guo, Synthesis and photoelectrocatalytic activity of In_2O_3 hollow microspheres via a bio-template route using yeast templates, Dalton Trans. 47 (2018) 708–715.

[46] X. Yang, X. Song, Y. Wei, W. Wei, L. Hou, X. Fan, Synthesis of spinous ZrO_2 core–shell microspheres with good hydrogen storage properties by the pollen bio-template route, Scripta Mater. 64 (2011) 1075–1078.

[47] J. Zhao, S. Ge, L. Liu, Q. Shao, X. Mai, C.X. Zhao, L. Hao, T. Wu, Z. Yu, Z. Guo, Microwave solvothermal fabrication of zirconia hollow microspheres with different morphologies using pollen templates and their dye adsorption removal, Ind. Eng. Chem. Res. 57 (2017) 231–241.
[48] H. Choi, A.C. Sofranko, D.D. Dionysiou, Nanocrystalline TiO_2 photocatalytic membranes with a hierarchical mesoporous multilayer structure: synthesis, characterization, and multifunction, Adv. Funct. Mater. 16 (2006) 1067–1074.
[49] K. Kočí, L. Matějová, M. Reli, L. Čapek, V. Matějka, Z. Lacný, P. Kustrowski, L. Obalová, Sol–gel derived Pd supported TiO_2-ZrO_2 and TiO_2 photocatalysts; their examination in photocatalytic reduction of carbon dioxide, Catal. Today 230 (2014) 20–26.
[50] H. Chen, G. Jiang, T. Jiang, L. Li, Y. Liu, Q. Huang, W. Chen, Preparation of Mn-doped ZrO_2/TiO_2 photocatalysts for efficient degradation of Rhodamine B, MRS Commun. 5 (2015) 1–7.
[51] S.A.K. Jalili, B. Mirza, Sonosynthesis and characterization of TiO_2/ZrO_2 nanocomposite and photocatalytic degradation of congo red dye under UV Light, J. Chem. Res. 10 (2016) 123–133.
[52] J.J. Schneider, M. Naumann, Template-directed synthesis and characterization of microstructured ceramic Ce/ZrO_2-SiO_2 composite tubes, Beilstein J. Nanotech. 5 (2014) 1152–1159.
[53] J. Wang, J. Huang, J. Meng, Q. Li, J. Yang, Double-hole codoped huge-gap semiconductor ZrO_2 for visible-light photocatalysis, Phys. Chem. Chem. Phys. 18 (2016) 17517–17524.
[54] M. Sevilla, A.B. Fuertes, Catalytic graphitization of templated mesoporous carbons, Carbon 44 (2006) 468.
[55] J.L.F. Schulte, U. Panne, J. Kneipp, Chemical characterization and classification of pollen, Anal. Chem. 80 (2008) 9551–9556.
[56] M.A. Behnajady, N. Modirshahla, M. Shokri, Photodestruction of Acid Orange 7 (AO7) in aqueous solutions by UV/H_2O_2: influence of operational parameters, Chemosphere 55 (2004) 129–134.
[57] T. Tachikawa, A.M. Fujitsuka, T. Majima, Mechanistic insight into the TiO_2 photocatalytic reactions: design of new photocatalysts, J. Phys. Chem. C 111 (2007) 5259–5275.
[58] L. Zhang, W. Yu, C. Han, J. Guo, Q. Zhang, H. Xie, Q. Shao, Z. Sun, Z. Guo, Large scaled synthesis of heterostructured electrospun TiO_2/SnO_2 nanofibers with an enhanced photocatalytic activity, J. Electrochem. Soc. 164 (2017) H651–H656.
[59] Y. Guo, G. Xu, X. Yang, K. Ruan, T. Ma, Q. Zhang, J. Gu, Y. Wu, H. Liu, Z. Guo, Significantly enhanced and precisely modeled thermal conductivity in polyimide nanocomposites by chemically modified graphene via in-situ polymerization and electrospinning-hot press technology, J. Mater. Chem. C 6 (2018) 3004–3015.
[60] J. Gu, W. Dong, Y. Tang, Y. Guo, L. Tang, J. Kong, S. Tadakamalla, B. Wang, Z. Guo, Ultra-low dielectric, fluoride-containing cyanate ester resins combining with prominent mechanical properties and excellent thermal and dimension stabilities, J. Mater. Chem. C 5 (2017) 6929–6936.
[61] P. Xie, Z. Wang, Z. Zhang, R. Fan, C. Cheng, H. Liu, Y. Liu, T. Li, C. Yan, N. Wang, Z. Guo, Silica microspheres templated self-assembly of three-dimensional carbon network with stable radio-frequency negative permittivity and low dielectric loss, J. Mater. Chem. C 6 (2018) 5239–5249.
[62] K. Sun, R. Fan, X. Zhang, Z. Zhang, Z. Shi, N. Wang, P. Xie, Z. Wang, G. Fan, H. Liu, C. Liu, T. Li, C. Yan, Z. Guo, An overview of metamaterials and their achievements in wireless power transfer, J. Mater. Chem. C 6 (2018) 2925–2943.
[63] K. Gong, Q. Hu, Y. Xiao, X. Cheng, H. Liu, N. Wang, B. Qiu, Z. Guo, Triple layered core-shell ZVI@carbon@polyaniline composites enhanced electron utilization in Cr(VI) reduction, J. Mater. Chem. A (2018), https://doi.org/10.1039/C8TA6A. in press.
[64] Q. Luo, H. Ma, Q. Hou, Y. Li, J. Ren, X. Dai, Z. Yao, Y. Zhou, L. Xiang, H. Du, H. He, N. Wang, K. Jiang, H. Lin, H. Zhang, Z. Guo, All-carbon-electrode-based endurable flexible perovskite solar cells, Adv. Func. Mater. 28 (2018) 1706777.
[65] Y. Ding, B. Yang, H. Liu, Z. Liu, X. Zhang, X. Zheng, Q. Liu, FePt-Au ternary metallic nanoparticles with the enhanced peroxidase-like activity for ultrafast colorimetric detection of H_2O_2, Sens. Actuat. B: Chem. 259 (2018) 775–783.
[66] Z. Hu, Q. Shao, Y. Huang, L. Yu, D. Zhang, X. Xu, J. Lin, H. Liu, Z. Guo, Light triggered interfacial damage self-healing of poly(p- phenylene benzobisoxazole) fiber composites, Nanotechnology 29 (2018) 185602.
[67] X. Wang, X. Liu, H. Yuan, et al., Non-covalently functionalized graphene strengthened poly(vinyl alcohol), Mater. Design 139 (2018) 372–379.
[68] W. Deng, T. Kang, H. Liu, et al., Potassium hydroxide activated and nitrogen doped graphene with enhanced supercapacitive behavior, Sci. Adv. Mater. 10 (2018) 937–949.
[69] L. Gao, L. Zhang, X. Lyu, G. Lu, Q. Liu, Corrole functionalized iron oxide nanocomposites as enhanced peroxidase mimic and their application in H_2O_2 and glucose colorimetric sensing, Eng. Sci. 1 (2018) 69–77.
[70] H. Du, C. Zhao, J. Lin, et al., Carbon nanomaterials in direct liquid fuel cells, Chem. Record (2018), https://doi.org/10.1002/tcr.201800008. in press.
[71] J. Huang, Y. Cao, Q. Shao, X. Peng, Z. Guo, Magnetic nanocarbon adsorbents with enhanced hexavalent chromium removal: morphology dependence of fibrillar vs particulate structures, Ind. Eng. Chem. Res. 56 (2017) 10689–10701.